Adsorption
https://doi.org/10.1007/s10450-024-00444-z

Comparison of 3D-cDFT and GCMC simulations for fluid–structure analysis in amorphous carbon nanoporous materials

Lucas J. dos Santos[1] · Elvis do A. Soares[1] · Amaro G. Barreto Jr.[1] · Frederico W. Tavares[1,2]

Received: 15 July 2023 / Revised: 27 October 2023 / Accepted: 23 February 2024

Abstract
Investigating fluid behavior in nanoporous materials is essential for gas storage, separation, and catalysis applications. Here, we present a comparison of two computational methods for fluid–structure analysis in amorphous nanoporous carbon materials: three-dimensional (3D) classical density functional theory (cDFT) and grand canonical Monte Carlo (GCMC) simulations. We extended our recent development of 3D-cDFT to allow density-profile analysis without symmetry assumptions, enhancing its applicability to a broader range of porous materials. We provide a theoretical overview and discuss the advantages and limitations of each method. Our results highlight the accuracy of both 3D-cDFT and GCMC simulations while emphasizing differences in computational cost, precision, and scope. We also explore the impact of the non-crystalline structure of amorphous carbon nanopores on fluid structure and adsorption isotherms, as well as fluid–fluid and fluid–solid interactions. We offer insights for selecting computational methods in fluid structure analysis of nanoporous materials, guiding future research and optimization in advanced material development for diverse applications.

Keywords Amorphous materials · Nanoporous carbon · Asymmetric structure · 3D · cDFT

1 Introduction

Due to their excellent surface activity [20], nanoporous carbonaceous materials, including activated carbons, carbon fibers, and carbon molecular sieves, are widely used in various industrial applications such as mixture separations [50], water purification [2], CO_2 capture [36, 68, 79], electrodes [42, 52, 85], hydrogen [32] and natural gas storage [16]. Achieving success in these applications relies heavily on developing and characterizing nanoporous carbons.

In recent years, molecular simulations and classical density functional theory (cDFT) calculations have provided insights into the behavior of gases and fluids within these carbon materials. Since the seminal work of [72], much of this work has focused on one-dimensional (1D) nanopore geometries, offering a simplified yet informative perspective on the adsorption and transport phenomena within this nanoporous structures [81, 82]. These methodologies have proven effective in capturing the essential physics of adsorption and have provided a platform for predicting material performance under various conditions.

However, real-world nanoporous carbon materials often exhibit three-dimensional (3D) geometries with no inherent symmetry, which presents a more complex scenario. Unlike crystalline solids, such as zeolites [22, 33, 34, 75] and metal–organic frameworks (MOFs) [15, 59], with regular and well-defined structures, nanoporous carbons consist of disordered graphitic domains. This amorphous structure results in highly convoluted internal surfaces and pores of diverse shapes and sizes, creating a disordered 3D pore network. The accuracy of 1D models in accounting for adsorption is insufficient, mainly when predicting the heat of adsorption and diffusion in these materials [8]. In this sense, extracting atomically detailed structures from amorphous materials presents a challenge. Creating realistic structural models is crucial for characterizing the pore structure and

Special Issue: EBA14—14th Brazilian Meeting on Adsorption.

✉ Frederico W. Tavares
tavares@eq.ufrj.br

[1] Engenharia de Processos Químicos e Bioquímicos (EPQB), Escola de Química, Universidade Federal do Rio de Janeiro, Rio de Janeiro, RJ 21941-909, Brazil

[2] Programa de Engenharia Química, COPPE, Universidade Federal do Rio de Janeiro, Rio de Janeiro, RJ 21941-909, Brazil

Published online: 16 April 2024

predicting the adsorption of different gases and their mixtures across many thermodynamic conditions.

In recent work, [9] used molecular models of nanoporous carbons for pore structure characterization and simulations of the adsorption of simple fluids and hydrocarbons using GCMC, demonstrating the advantages and capabilities of using 3D models. There are two methods based on molecular simulation for generating molecular models of nanoporous carbons: hybrid reverse Monte Carlo (HRMC) and molecular dynamics (MD). HRMC combines the features of the Monte Carlo (MC) and Reverse Monte Carlo (RMC) [41] methods in order to reproduce the experimental pair distribution function of the material of interest [27]. Different approaches use MD, such as Quench Molecular Dynamics (QMD) [47, 48] and Annealed MD (AMD) [12, 13]. Using AMD simulations, [80] generated a database of 3D carbon structures, encompassing a wide range of pore sizes and geometries, and calculated adsorption isotherms via GCMC. Through this kernel, the authors were able to find the relative contributions of each of these structures in experimentally measured isotherms and to estimate the surface area and pore size distribution.

The cDFT is a theoretical framework that describes the spatial distribution of fluid molecules inside a porous material based on the minimization of a free energy functional of the density field. Previous research within this field has focused primarily on symmetrical geometries to describe the adsorption of gases within nanoporous carbon materials [3, 53, 55, 56, 62, 63, 66]. This approach, while useful in certain contexts, may not fully capture the complexity and diversity of real-world scenarios, given the inherently disordered and asymmetrical nature of nanoporous carbon structures. The unique characteristics of these materials, including their varied pore sizes and shapes, and the tortuous pathways within, necessitate a more nuanced approach for accurate representation and prediction of gas adsorption behavior.

[54] proposed the Quenched Solid Density Functional Theory (QSDFT) for modeling adsorption in heterogeneous materials with corrugated amorphous walls applied to siliceous materials. [44] extended to adsorption on nanoporous carbons. [64] expanded upon this model using a functional based on the PC-SAFT equation of state to study the adsorption of methane, ethane, propane, and butane on carbonaceous pores. [26] used two-dimensional (2D) cDFT to calculate adsorption on activated carbons by introducing a spatial function for modeling surface roughness and chemical heterogeneity. [67] studied the effects of energetic heterogeneities on the adsorption mechanism fluids (modeled by a functional based on the PC-SAFT equation of state), simulating heterogeneous carbonaceous cavities considering a sinusoidal perturbation on the external potential.

In recent years, advancements in cDFT, particularly in the development of three-dimensional (3D) cDFT, have enhanced its capacity to model density profiles without relying on symmetry assumptions. These improvements have broadened the applicability to a wider range of crystalline porous materials, including MOFs, while maintaining its computational efficiency [6, 18, 19, 30, 61]. On the other hand, GCMC simulations have remained a popular choice for researchers due to their flexibility in modeling fluid behavior, enabling them to capture complex interactions between gases such as methane, nitrogen, and carbon dioxide inside crystalline nanoporous materials like MOFs [35, 76, 77]. As an example, recently, [71] presented 3D-cDFT calculations for the adsorption of CH_4 and H_2 inside the crystalline MOF-5 3D structure. Extending the current methodologies from 1D to 3D geometries is a challenging but necessary step to accurately represent non-crystalline materials and predict their adsorption behavior. This paper aims to address this gap, extending the application of 3D-cDFT calculations to amorphous nanoporous carbon materials without any symmetry assumption.

This work aims to demonstrate the applicability of 3D-cDFT calculations and GCMC simulations for methane inside these amorphous nanoporous carbon materials. To offer a comparative analysis of the accuracy, and computational cost of 3D-cDFT calculations and GCMC simulations, we will present case studies examining two different carbon nanoporous materials and their interactions with methane molecules. These case studies will highlight the differences between the two methods in terms of their ability to model fluid behavior under different thermodynamic conditions.

Following this section, Sect. 2 presents a brief background regarding the implementation of the GCMC and the cDFT and their application for describing gas adsorption in 3D geometries. The discussion of the results from these methods is performed in Sect. 3. Finally, Sect. 4 presents the conclusions of this work.

2 Theory and methods

2.1 Classical density functional theory

The cDFT is based on the fact that the grand thermodynamic potential, $\Omega[\rho(\boldsymbol{r})]$, and the Helmholtz free-energy, $F[\rho(\boldsymbol{r})]$, can be written as functionals of the density distribution of the fluid, $\rho(\boldsymbol{r})$ [17, 23, 24, 83]. The grand potential functional $\Omega[\rho(\boldsymbol{r})]$ is related to the free energy functional $F[\rho(\boldsymbol{r})]$ by a thermodynamic relation given as

$$\Omega[\rho(\boldsymbol{r})] = F[\rho(\boldsymbol{r})] + \int_V d\boldsymbol{r}[\phi_{\text{ext}}(\boldsymbol{r}) - \mu]\rho(\boldsymbol{r}), \tag{1}$$

where μ is the equilibrium chemical potential and $\phi_{\text{ext}}(\boldsymbol{r})$ is an external potential acting on the fluid. The Helmholtz free

energy functional is determined by the sum of two terms, in the form

$$F[\rho(\boldsymbol{r})] = F_{\text{id}}[\rho(\boldsymbol{r})] + F_{\text{exc}}[\rho(\boldsymbol{r})], \tag{2}$$

where the first term is the ideal gas contribution and the second term is the excess free energy parcel (excess of ideal gas). The ideal-gas contribution F^{id} is given by the exact expression

$$F^{\text{id}}[\rho(\boldsymbol{r})] = k_B T \int_V d\boldsymbol{r}\rho(\boldsymbol{r})[\ln(\rho(\boldsymbol{r})\Lambda^3) - 1], \tag{3}$$

where k_B is the Boltzmann constant, T is the absolute temperature, and Λ is the well-known thermal de Broglie wavelength.

The excess free energy functional $F_{\text{exc}}[\rho(\boldsymbol{r})]$ contains all the information about the interaction between particles given by the pair potential $u(\boldsymbol{r}-\boldsymbol{r}')$. In our problem, the molecule-molecule interactions of the fluid can be well described by the Lennard–Jones potential in the form

$$u_{\text{lj}}(r) = 4\epsilon\left[\left(\frac{\sigma}{r}\right)^{12} - \left(\frac{\sigma}{r}\right)^{6}\right]. \tag{4}$$

Following our previous work [71] in 3D-cDFT, the excess free energy is split into repulsive and attractive contributions, F_{rep} and F_{att}, respectively, such that

$$F_{\text{exc}}[\rho(\boldsymbol{r})] = F_{\text{rep}}[\rho(\boldsymbol{r})] + F_{\text{att}}[\rho(\boldsymbol{r})]. \tag{5}$$

The repulsive term F_{rep} in Eq. (5) can be modeled by the free energy functional of a reference hard-sphere fluid [31] defined by a short-range hard-sphere interaction with an effective diameter for the hard-core region described by Barker and Henderson's [4, 5, 10] temperature-dependent diameter, denominated d. The modified fundamental measure theory (FMT) [57] accurately describes the hard-sphere fluid structures and can represent the hard-sphere free energy functional, $F_{\text{hs}}[\rho(\boldsymbol{r})]$. In this work, we have applied the antisymmetrized version of the White-Bear functional [58, 87] for the hard-sphere Helmholtz free energy contribution as

$$\begin{aligned} F_{\text{rep}}[\rho(\boldsymbol{r})] &= F_{\text{hs}}[\rho(\boldsymbol{r})] \\ &= k_B T \int_V d\boldsymbol{r}\Phi_{\text{FMT}}(\{n^{(\alpha)}(\boldsymbol{r})\}), \end{aligned} \tag{6}$$

where Φ_{FMT} is the local reduced free energy density of a mixture of hard spheres, a function of the set of weighted densities, $n^{(\alpha)}(\boldsymbol{r})$. The FMT functional and the weighted densities are defined in Ref. [60].

The attractive term F_{att} in Eq. (5) represents the excess Helmholtz free energy contribution due to the particle-particle attractive interaction defined by the potential

$$u_{\text{att}}(r) = \begin{cases} 0, & r < \sigma, \\ -\epsilon_1 \frac{e^{-\lambda_1(r/\sigma-1)}}{r/\sigma} - \epsilon_2 \frac{e^{-\lambda_2(r/\sigma-1)}}{r/\sigma}, & r > \sigma, \end{cases} \tag{7}$$

with $\epsilon_1 = -\epsilon_2 = 1.8577\epsilon$, $\lambda_1 = 2.5449$, and $\lambda_2 = 15.4641$. The attractive parcel of the LJ potential was mapped onto a Two-Yukawa potential, as proposed previously [29, 73, 74] to facilitate the Fourier Transform on the numerical calculations. The free energy functional $F_{\text{att}}[\rho(\boldsymbol{r})]$ can be described by the novel weighted density functional theory (WDFT) [86] as the sum of a mean-field term and a correlation contribution, respectively, in the form

$$\begin{aligned} F_{\text{att}}[\rho(\boldsymbol{r})] = \frac{1}{2}\int_V d\boldsymbol{r}\int_V d\boldsymbol{r}'\rho(\boldsymbol{r})u_{\text{att}}(|\boldsymbol{r}-\boldsymbol{r}'|)\rho(\boldsymbol{r}') \\ + k_B T \int_V d\boldsymbol{r}\Phi_{\text{corr}}(\bar{\rho}(\boldsymbol{r})), \end{aligned} \tag{8}$$

where the weighted density field here is given by $\bar{\rho}(\boldsymbol{r}) = \int_V d\boldsymbol{r}'\rho(\boldsymbol{r}')\omega_{\text{wdft}}(\boldsymbol{r}-\boldsymbol{r}')$ with $\omega_{\text{wdft}}(\boldsymbol{r}) = \Theta(d-|\boldsymbol{r}|)/(4\pi d^3/3)$, and $\Theta(x)$ is the Heaviside function. The correlation free energy density is fully described in Ref. [71, 86].

Here, the Johnson, Zollweg, and Gubbins (JZG) equation of state for LJ fluids was employed [28]. While this equation has been shown to be highly accurate, it is important to note that it is a semi-empirical relation obtained from MD simulations with universal parameters. This EoS is written as

$$\frac{F_{\text{JZG}}(\rho)}{V} = \rho\epsilon\sum_{i=1}^{8}\frac{a_i(\rho\sigma^3)^i}{i} + \rho\epsilon\sum_{i=1}^{6} b_i G_i \tag{9}$$

where a_i and b_i are coefficients functions of temperature only. As reported in the original paper, the G_i functions contain exponentials of the density and the one nonlinear parameter. The CH_4 fluid-fluid interactions are described by the LJ potential with the parameters given in Table 1. The choice of TraPPE parameters is discussed in Supporting Information. The mapping of the equation of state is presented by the solid lines in Fig. 1 for CH_4 fluid, where the symbols are our GCMC simulated data.

The total external potential produced by the solid atoms on the fluid molecules is represented as a sum of the Lennard–Jones interaction between the solid atoms and the fluid molecules as defined following

$$\phi_{\text{ext}}(\boldsymbol{r}) = \sum_{i\in\text{ solid}} u_{if}^{(\text{lj})}(|\boldsymbol{r}-\boldsymbol{r}_i|) \tag{10}$$

with the mixed parameters obtained by the Lorentz-Berthelot combining rules, given by $\sigma_{if} = \frac{1}{2}(\sigma_{ii}+\sigma_{ff})$ and $\epsilon_{if} = (\epsilon_{ii}\epsilon_{ff})^{1/2}$. The LJ parameters for the carbon (C) atoms are given in Table 1. In order to align with the periodic boundary conditions, we replicate the solid unit cell into a $3\times3\times3$ supercell. As defined by Eq. (10), the external

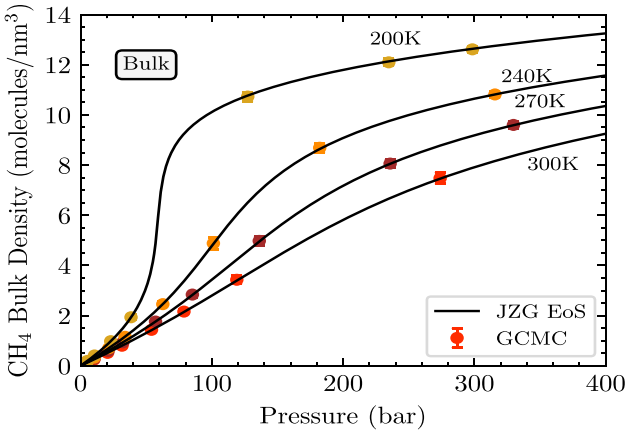

Fig. 1 Equation of state of bulk CH_4 fluid over a broad pressure and temperature range. Open symbols: Our simulated GCMC data. Solid lines: JZG EoS with LJ parameters from Table 1

Table 1 LJ parameters of the components

Component	ϵ/k_B (K)	σ (Å)	Model
CH_4	148.0	3.73	TraPPE[a]
C	47.856	3.473	DREIDING[b]

[a]Ref. [39]

[b]Ref. [40]

potential is computed as being generated by all atoms within the supercell in the centrally located unit cell.

The grand potential $\Omega[\rho(\boldsymbol{r})]$ has a minimum value when $\rho(\boldsymbol{r})$ is the equilibrium density distribution, i.e., the minimum value of $\Omega[\rho(\boldsymbol{r})]$ is the equilibrium grand potential of the system. Then, the equilibrium density profile can be calculated by the extremum of the grand canonical potential, such that (see the detailed derivation in the Supporting Information document)

$$\left.\frac{\delta\Omega[\rho(\boldsymbol{r})]}{\delta\rho(\boldsymbol{r})}\right|_{\mu,V,T} = k_BT\ln(\rho(\boldsymbol{r})\Lambda^3) + \frac{\delta F_{\text{exc}}[\rho(\boldsymbol{r})]}{\delta\rho(\boldsymbol{r})} + \phi_{\text{ext}}(\boldsymbol{r}) - \mu = 0. \tag{11}$$

Using the definition of the chemical potential in the form $\mu = k_BT\ln(\rho_b\Lambda^3) + \mu_{\text{exc}}$, where ρ_b is the uniform fluid bulk density and μ_{exc} is the excess chemical potential, we can write the simplified form of Eq. (11) as

$$\rho(\boldsymbol{r}) = \rho_b\exp[-\beta\phi_{\text{ext}}(\boldsymbol{r}) + c^{(1)}(\boldsymbol{r}) + \beta\mu_{\text{exc}}], \tag{12}$$

where $\beta = (k_BT)^{-1}$ is the inverse of the thermal energy, and the term $c^{(1)}(\boldsymbol{r})$ is the first-order direct correlation function defined through the relation $c^{(1)}(\boldsymbol{r}) = -\beta\delta F_{\text{exc}}[\rho(\boldsymbol{r})]/\delta\rho(\boldsymbol{r})$. The sum $c^{(1)}(\boldsymbol{r}) + \beta\mu_{\text{exc}}$ acts as a effective potential correcting the external potential $\phi_{\text{ext}}(\boldsymbol{r})$ due to the fluid-fluid correlation. In our specific case, the local density field is a 3D field, which necessitates the utilization of isosurfaces to visualize our cDFT results.

Finally, the absolute adsorption quantity can be calculated by definition as

$$N_{\text{abs}} = \int_{V_{\text{uc}}}\rho(\boldsymbol{r})d\boldsymbol{r}, \tag{13}$$

where the local density distribution $\rho(\boldsymbol{r})$ is given by Eq. (12). We can also define the mean density inside the nanoporous material by the relation

$$\rho_{\text{abs}} = \frac{N_{\text{abs}}}{V_{\text{uc}}}, \tag{14}$$

where V_{uc} is the volume of the unit cell.

To speed up the numerical calculations, we used the fast fourier transform (FFT) to calculate all the necessary convolutions. All the numerical FFT convolutions are calculated using the *PyTorch* package [49] with GPU acceleration. Our group implemented the FMT and WDFT functionals in *Python* code. [70] The Gibbs phenomenon was reduced by multiplicating the Fourier transform $\tilde{\omega}_\alpha(\boldsymbol{k})$ by the Lanczos σ -factor, $\sigma(k) = \sin(k/k_{\max})/(k/k_{\max})$, where $k_{\max}$ is the maximum wavenumber from the FFT procedure.

The equilibrium condition of the cDFT, Eq. (11), is solved using an Accelerated Bias-Corrected Fast Inertial Relaxation Engine (ABC-FIRE) [7, 14, 21] also implemented in *Python* by our group [65, 69]. The ABC-FIRE parameters are set as $\alpha = 0.2$ and $dt = 0.002$. The algorithm convergence criterion is

$$\frac{1}{\sqrt{N_xN_yN_z}}\left\|\frac{\beta\delta\Omega/\delta\rho(\boldsymbol{r})}{(atol + rtol|\rho(\boldsymbol{r})|)}\right\|_F \leq 1, \tag{15}$$

with $atol = 10^{-6}$ and $rtol = 10^{-4}$, where $\|A\|_F$ is the Frobenius norm.

The initial density was considered uniform and equal to the bulk density value, ρ_b. In the highly repulsive region, where $\phi_{\text{ext}}(\boldsymbol{r})/k_B > 1.6\times10^4$ K, the initial density $\rho(\boldsymbol{r})$ was assumed to be zero. For the adsorption isotherm calculations, the density profile obtained at the previous pressure step is used as the initial profile of the next pressure step. We have used a pressure step of 0.01 bar from 0.001 bar to 1.0 bar, a step of 0.1 bar from 1 bar to 10 bar, a step of 0.5 bar from 10 bar to 150 bar, and a step of 5 bar from 150 bar to 500 bar.

2.2 Grand canonical Monte Carlo

All GCMC simulations were performed using the open-source software GPU Optimized Monte Carlo (GOMC) [45]. The files required by GOMC for the simulations were generated using the MoSDeF-GOMC package [11]. Methane

molecules were described as LJ spheres using parameters from Table 1. The carbon structures were considered rigid, and the carbon atoms that compose them have also been described as LJ spheres, with the parameters given in Table 1. Parameters for the solid–fluid interactions were calculated using Lorentz–Berthelot combining rules. A 14 Å cut-off radius and long-range corrections for LJ interactions were used for all calculations.

The adsorption isotherms were calculated with 40×10^6 Monte Carlo steps, 10×10^6 for equilibration and 30×10^6 for production, at 200 K, 240 K, 270 K, and 300 K. In order to conduct simulations at constant chemical potential, the pressures were pre-computed through GCMC simulations for the bulk fluid, as presented in Fig. 1.

2.3 Amorphous carbon nanostructures

Figure 2 shows the two carbon structures taken from the database of porous rigid amorphous materials [78]: aCarbon-Bhatia-id001 [46], and aCarbon-Marks-id002 [51].

The first, aCarbon-Bhatia-id001, is an atomistic model of the structure of an ACF15 activate carbon generated by HRMC using the experimental pair distribution function of the material obtained by X-ray diffraction [46]. The second was generated by MD using the environment-dependent interaction potential (EDIP) [37, 38]. Starting from an amorphous carbon precursor generated by liquid quenching [37], an annealing simulation is performed at 4000 K to obtain the final structure [51].

Our cDFT calculations are made using the number of grid points of $N^3 = 32^3$ and $N^3 = 64^3$. For the cases studied here, the results with a larger number of grid points, e.g., $N^3 = 128^3$, are identical to the results with $N^3 = 64^3$. As the aCarbon-Bhatia-id001 has a lattice length of $L = (2.95\ \text{nm}, 2.98\ \text{nm}, 3.02\ \text{nm})$ with the unit cell volume of $V_{\text{uc}} = L_x L_y L_z = 26.55\ \text{nm}^3$, the corresponding grid sizes are related to the molecule diameter as shown in Table 2 for the CH_4 molecule. For the aCarbon-Marks-id002, the lattice lengths are $L = (3.79\ \text{nm}, 3.79\ \text{nm}, 3.79\ \text{nm})$ with a unit cell volume of $V_{\text{uc}} = 54.44\ \text{nm}^3$, and the corresponding grid sizes are also presented in Table 2. Our systematic evaluations indicate that a grid size below $0.25\sigma_{ff}$ is most suitable for the cDFT calculations.

3 Results and discussion

Figure 3 illustrates the absolute isotherms of CH_4 adsorption on aCarbon-Bhatia-id001 at temperatures of 200 K, 240 K, 270 K, and 300 K. Symbols represent the GCMC simulation data, while the 3D-cDFT results are presented as dashed and solid lines. The data are given in the supplementary information (Tables S1–S4). The no-correlation approximation, with the local density given by $\rho(\boldsymbol{r}) = \rho_b \exp(-\beta\phi_{\text{ext}}(\boldsymbol{r}) + \beta\mu_{\text{exc}})$, is shown as dotted lines. This approximation is sometimes denominated ideal because there is no contribution from the excess free energy functional at the adsorbed phase, although the excess quantities are present in the bulk phase [84]. The

Table 2 Relative grid size used to calculate the adsorption isotherm of CH_4 in a carbon nanostructures with 3D-cDFT

Model	N^3	$[\Delta x/\sigma_{ff}, \Delta y/\sigma_{ff}, \Delta z/\sigma_{ff}]$
Bhatia-id001	32^3	[0.247, 0.250, 0.253]
	64^3	[0.124, 0.125, 0.127]
Marks-id002	32^3	[0.318, 0.318, 0.318]
	64^3	[0.159, 0.159, 0.159]

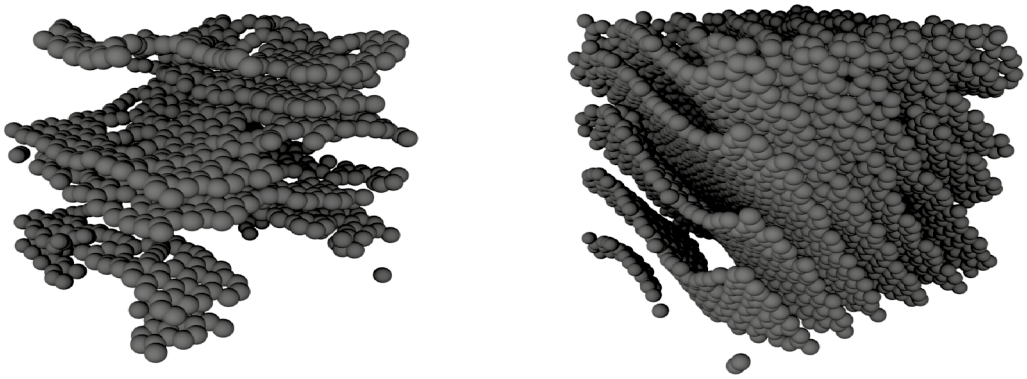

(a) aCarbon-Bhatia-id001 (b) aCarbon-Marks-id002

Fig. 2 Carbon structures: **a** aCarbon-Bhatia-id001 [46] (29.5 Å × 29.8 Å × 30.2 Å, 1166 atoms), **b** aCarbon-Marks-id002 [51] (37.9 Å × 37.9 Å × 37.9 Å, 4096 atoms)

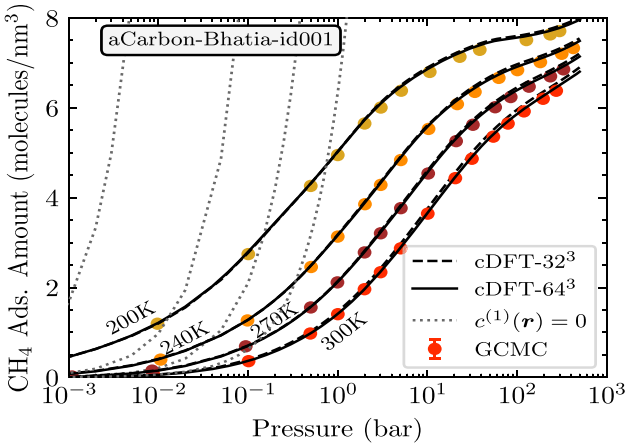

Fig. 3 Isotherms of the absolute adsorption amount of CH_4 in aCarbon-Bhatia-id001 at temperature values of 200 K, 240 K, 270 K, and 300 K and a wide pressure range in logarithmic scale. Closed symbols: Our GCMC simulated data. Dotted lines: No-correlation model. Dashed lines: Our cDFT results with $N^3 = 32^3$. Solid lines: Our cDFT results with $N^3 = 64^3$

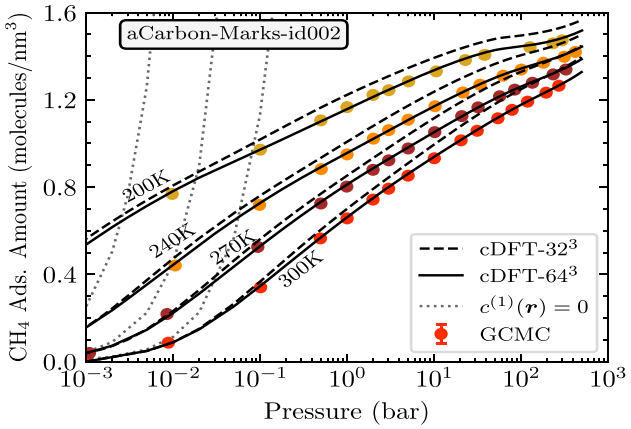

Fig. 4 Isotherms of the absolute adsorption amount of CH_4 in aCarbon-Marks-id002 at temperature values of 200 K, 240 K, 270 K, and 300 K and a wide pressure range in logarithmic scale. Closed symbols: Our GCMC simulated data. Dotted lines: No-correlation model. Dashed lines: Our cDFT results with $N^3 = 32^3$. Solid lines: Our cDFT results with $N^3 = 64^3$

curves reveal a steady increase in the amount of CH_4 adsorption as pressure rises at each temperature. There is a remarkable consistency between the cDFT results and GCMC data across the entire pressure range and at all temperatures. However, as expected, the ideal gas approximation cannot describe the isotherm curves for higher pressure values. This limitation arises from the significant role of fluid-fluid correlations for the CH_4 fluid within this solid. For example, at 300 K the fluid-fluid correlations are very important at pressures exceeding 0.1 bar. Moreover, there is no noticeable disparity between the results when comparing the number of grid points of $N^3 = 32^3$ and $N^3 = 64^3$.

Similarly, Fig. 4 shows the absolute isotherms of CH_4 adsorption on aCarbon-Marks-id002 at 200 K, 240 K, 270 K, and 300 K. The data are given in the supplementary information (Tables S5–S8). There is an excellent agreement between the results obtained by the two methods over the entire pressure range and for all temperatures using $N^3 = 64^3$ grid points. The cDFT calculations with $N^3 = 64^3$ perform better than the cDFT calculations using $N^3 = 32^3$, mainly at high-pressure regions when compared to the GCMC simulation data. In fact, the cDFT with $N^3 = 32^3$ overestimating the amount adsorbed.

Upon examining the results presented in Figs. 3 and 4, it becomes apparent that the aCarbon-Bhatia-id001 material exhibits a higher adsorption quantity of CH_4 compared to aCarbon-Marks-id002, despite the latter having a larger unit-cell volume. The unit-cell volume of the Carbon-Marks-id002 structure is nearly twice that of the Carbon-Bhatia-id001 structure. However, the former structure contains approximately four times as many carbon atoms as the latter structure. Thus, the discrepancy in adsorption quantities can be attributed to the differing solid densities of the two materials: the aCarbon-Bhatia-id001 has a density of 875.9 kg/m^3, while the aCarbon-Marks-id002 has a significantly higher density of 1500.6 kg/m^3.

We also can calculate the Helium (He) void fraction, $V_{\text{pore}}/V_{\text{uc}}$, where V_{pore} is the pore volume obtained by He pycnometry [43]. This pore volume also can be calculated by the 3D-cDFT as $V_{\text{pore}} = \int_{V_{\text{uc}}} \exp[-\beta\phi_{\text{ext}}^{(\text{He})}(\boldsymbol{r})]d\boldsymbol{r}$, with the He LJ parameters $\sigma_{\text{He}} = 2.58$ Å, $\epsilon_{\text{He}}/k_B = 10.22$ K) [25]. For the aCarbon-Bhatia-id001 structure, the helium void fraction is computed to be 0.711, while for aCarbon-Marks-id002, it is 0.292. These values are in accordance with those documented in Ref. [78], specifically 0.76 and 0.33, respectively. The reduced void fraction in aCarbon-Marks-id002 imposes a limitation on the adsorbed amount of CH_4 onto this structure. Furthermore, these findings underscore the importance of the fluid–fluid correlation effects generated by the exclusion volume phenomenon when performing adsorption calculations using 3D-cDFT in amorphous carbon nanoporous materials. We also present the isotherm curves of the excess adsorption in supplementary information (Figs. S2, S3).

It is important to note that GCMC calculations use periodic boundary conditions: the simulation box is replicated through space to form an infinity lattice [1]. In that way, using the same condition to calculate external potential in cDFT is necessary to obtain agreement between the results. Without this condition, cDFT underestimates the amount adsorbed. The main advantage of cDFT is computational time. In some instances, the time needed to calculate the entire isotherm is similar to the GCMC

time to calculate just one point of the isotherm. For these structures with many atoms, GCMC is quite exhaustive. At each step, all solid–fluid interactions need to be calculated. On the other hand, the external potential used in cDFT is calculated only once.

All calculations were performed on a regular desktop: Intel Core i7-11700 CPU, system's memory of 16 GB DDR4-RAM, GPU NVIDIA GeForce GTX 1050 Ti, and operational system Ubuntu 22.04 LTS. At 300 K, using a grid of $N^3 = 64^3$ points, the computational time required for determining the isotherm of CH_4 in aCarbon-Bhatia-id001 was 12 min and 45 s, considering 183 pressure values, while in aCarbon-Marks-id002 was 3 h and 21 min with 266 pressure values. In contrast, the GCMC method necessitated 48 min for calculating only the final point on the isotherm in aCarbon-Bhatia-id001, and 1 h and 55 min in aCarbon-Marks-id002.

A local density isosurface provides a three-dimensional visualization of points within a spatial volume with the same density value. Figures 5 and 6 display the local density isosurfaces of CH_4 in aCarbon-Bhatia-id001 and aCarbon-Marks-id002, respectively, at 300 K and at three distinct pressure values: 10 bar, 100 bar, and 300 bar. The isosurface in yellow means the region with a density of 1 molecule/nm^3, while the red isosurface represents a density of 100 molecules/nm^3. Given that aCarbon-Bhatia-id001 has a more substantial pore volume, more yellow regions are observable. Moreover, for this structure, the red regions, signifying higher density, expand in both number and area with increasing pressure. Conversely, for aCarbon-Marks-id002, the variations in the yellow and red regions are minimal due to the saturation of adsorption amount at lower pressures. Additional density isosurfaces are given in the supplementary information (Figs. S4, S5).

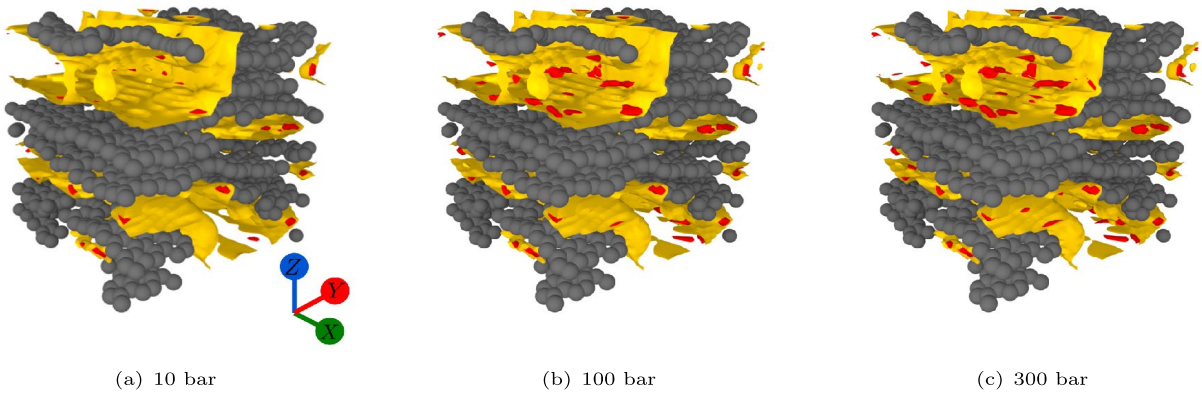

Fig. 5 Density isosurfaces of CH_4 in aCarbon-Bhatia-id001 with local density values of 1 molecules/nm^3 (yellow) and 100 molecules/nm^3 (red) at the temperature of 300 K and three different pressures of **a** 10 bar, **b** 100 bar and **c** 300 bar

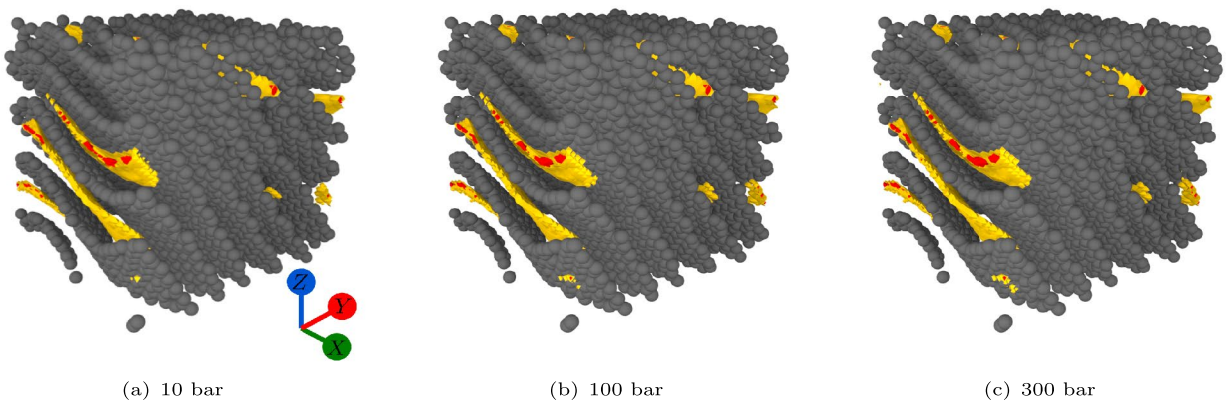

Fig. 6 Density isosurfaces of CH_4 in aCarbon-Marks-id002 with local density values of 1 molecules/nm^3 (yellow) and 100 molecules/nm^3 (red) at the temperature of 300 K and three different pressures of **a** 10 bar, **b** 100 bar and **c** 300 bar

The comparison of density profiles derived from GCMC simulations and cDFT calculations presents a significant challenge in three dimensions. Given that density is a scalar field dependent on three spatial coordinates, any attempt at three-dimensional visualization would inhibit a quantitative comparison. Hence, in this study, we opted to compare the marginalized distributions, which are defined based on the following relationship

$$\rho(x_1) = \iint \rho(x_1, x_2, x_3) dx_2 dx_3, \tag{16}$$

where the marginalized distribution $\rho(x_1)$ is only dependent of the coordinate x_1, and the integral in Eq. (16) is performed on the other two coordinates, named x_2 and x_3. Thereto, the integral $\int \rho(x_1) dx_1$ gives the total adsorbed amount of material as well as in Eq. (13).

Figure 7 displays the marginalized densities of CH_4 inside the aCarbon-Bhatia-id001 structure calculated at 300 K and 100 bar, facilitating a local comparison between the two methodologies. There is a strong correlation between the histogram of ρ generated by the GCMC simulation data and the marginalized densities derived from the local density distribution calculated with the 3D-cDFT.

Upon examining these profiles and comparing them with the information from the isosurfaces, as shown in Fig. 5, the symmetry of the aCarbon-Bhatia-id001 structure along the x-axis becomes evident, characterized by the nearly homogeneous density distribution. The marginalized density distribution on the y-axis has inhomogeneities. One example is a broad peak at $y \approx 13$ Å. The density distribution along the z-axis is more complex, featuring two narrow peaks around $z \approx 10$ Å and $z \approx 17$ Å. However, the remainder of the distribution in the z-axis appears to be a complex convolution of other peaks with varying thicknesses. There are two forbidden regions for the CH_4 molecules inside this structure along the z-axis located at $z \approx 13$ Å and $z \approx 19$ Å. These positions are correlated with the location of two graphene sheets inside the aCarbon-Bhatia-id001 structure, as we can visualize in Fig. 5.

Equivalently, Fig. 8 illustrates the marginalized densities of CH_4 within the aCarbon-Marks-id002 structure, calculated at 300 K and 100 bar. In this instance, all the marginalized distributions exhibit inhomogeneities. As anticipated, the values of the marginalized densities in aCarbon-Marks-id002 are lower than those in aCarbon-Bhatia-id001. There are also regions in the y-axis that are inaccessible to CH_4 molecules, represented by a broad region at $y \approx 12$ Å and a narrow region at $y \approx 24$ Å. The distributions in all directions exhibit the convolution of several peaks. In this case, there is no single direction where the marginalized distribution

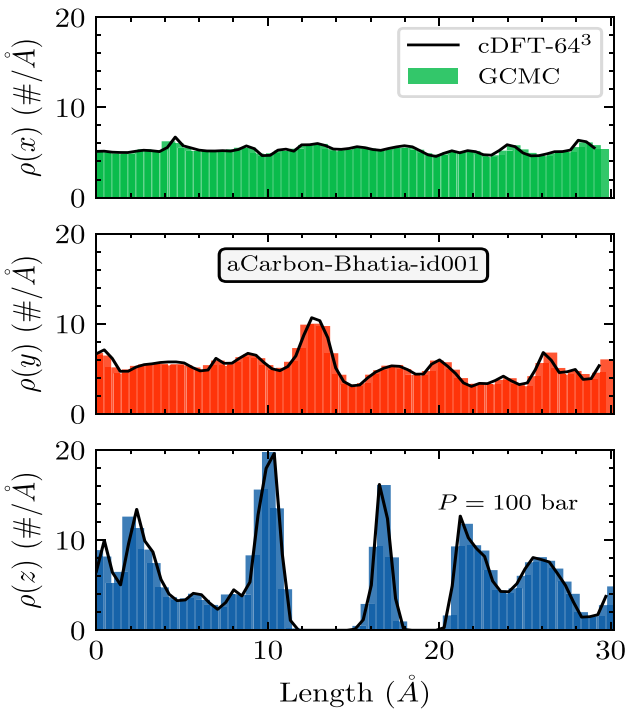

Fig. 7 Marginalized density distribution of CH_4 in aCarbon-Bhatia-id001 at the temperature of 300 K and the pressure of 100 bar. The unit #/Å corresponds to molecules/Å

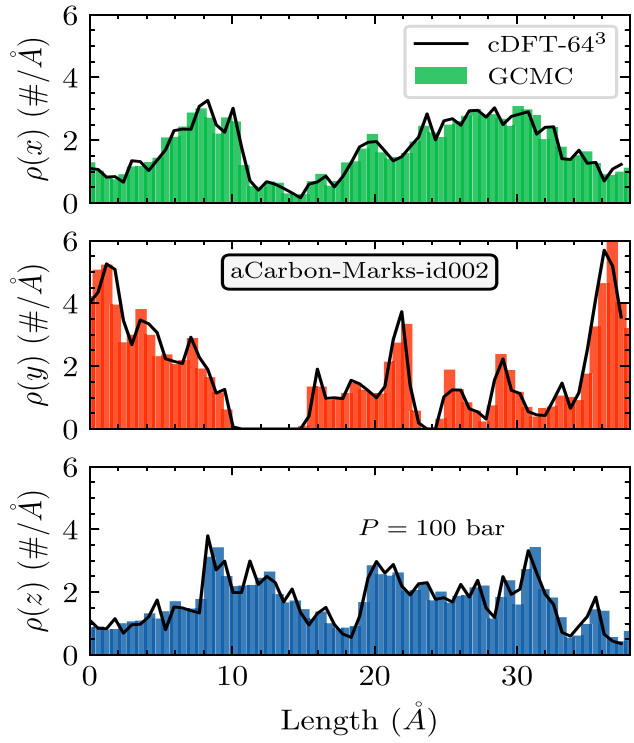

Fig. 8 Marginalized density distribution of CH_4 in aCarbon-Marks-id002 at the temperature of 300 K and the pressure of 100 bar. The unit #/Å corresponds to molecules/Å

approximates homogeneity. Interestingly, this structure is similar to stacked graphene sheets, with several defects. These defects are the most likely places to find CH_4 molecules, as shown in Fig. 6.

It is noticed that the representation of these structures using one-dimensional models, such as slit-shaped pores, fails. To accurately depict the fluid–structure in disordered carbon structures 3D model is needed. In such cases, the use of a simulated kernel of local isotherms in a series of independent slit-shaped pores to compute the pore size distribution in each of these directions merely results in a numerical fit. This approach is incapable of describing the asymmetry of the structure in the other directions, a feature that is characteristic of amorphous nanoporous carbons.

4 Conclusions

This study has provided a comprehensive examination of CH_4 adsorption in amorphous nanoporous carbon materials, specifically aCarbon-Bhatia-id001 and aCarbon-Marks-id002 (two molecular 3D models of nanoporous carbon) under varying conditions of temperature and pressure. Molecular simulations and cDFT calculations have proven instrumental in elucidating the fluid–structure inside these materials. However, the complexity of these materials, particularly their three-dimensional geometries and lack of symmetry, necessitates a more detailed approach.

The comparison of density profiles derived from GCMC simulations and cDFT calculations revealed the importance of considering fluid-fluid correlation effects when performing adsorption calculations. The results showed an excellent agreement between the two approaches for an extensive range of pressures ans temperatures. A more significant amount of CH_4 adsorption was observed inside the aCarbon-Bhatia-id001 material than in the aCarbon-Marks-id002, despite the latter having a larger unit-cell volume. This discrepancy can be attributed to the different solid densities and pore volumes of the two materials. Furthermore, the study highlighted the limitations of simplistic models, such as slit-shaped pores, in accurately representing fluid structure in disordered carbon structures. These findings underscore the need for more sophisticated methodologies like 3D-cDFT to describe nanoporous carbon materials.

5 Supplementary Information

The online version contains supplementary material available at https://link.springer.com/article

Derivation of the expression for the Grand Potential, and the derivation of Eq. (11). Excess adsorption isotherms and density isosurfaces of CH_4 inside aCarbon-Bhatia-id001 and aCarbon-Marks-id002. Tables of absolute adsorption data from GCMC simulations and cDFT calculations.

Supplementary Information The online version contains supplementary material available at https://doi.org/10.1007/s10450-024-00444-z.

Acknowledgements The authors thank Petrobras and Shell, which provided financial support through the Research, Development, and Innovation Investment Clause in collaboration with the Brazilian National Agency of Petroleum, Natural Gas, and Biofuels (ANP, Brazil). Additionally, this research was partially funded by CNPq, CAPES, and FAPERJ.

Author Contributions LS and ES wrote the original manuscript text. LS ran the molecular simulations and made cDFT calculations. ES made the cDFT calculations and prepared figures. AB and FT discussed the results and participated in the preparation and final revision of the manuscript. All authors reviewed the manuscript.

Funding No funding was received for conducting this study.

Data availability The data and code that support the findings of this study are available on the author's GitHub repository: https://github.com/elvissoares/PyDFTlj. No experimental data is provided.

Declarations

Conflict of interest The authors declare no competing financial interests.

Ethical approval Not applicable.

References

1. Allen, M.P., Tildesley, D.J.: Computer Simulation of Liquids. Oxford University Press, Oxford (2017)
2. An, N., Jiang, Y., Wang, Z., et al.: Efficient water purification and desalination using hydrogel and aerogel solar evaporators based on different carbon materials. Sep. Purif. Technol. **301**, 122003 (2022). https://doi.org/10.1016/j.seppur.2022.122003
3. Balbuena, P.B., Gubbins, K.E.: Theoretical interpretation of adsorption behavior of simple fluids in slit pores. Langmuir **9**(7), 1801–1814 (1993). https://doi.org/10.1021/la00031a031
4. Barker, J.A., Henderson, D.: Perturbation theory and equation of state for fluids. II. A successful theory of liquids. J. Chem. Phys. **47**(11), 4714–4721 (1967). https://doi.org/10.1063/1.1701689
5. Barker, J.A., Henderson, D.: Perturbation theory and equation of state for fluids: the square-well potential. J. Chem. Phys. **47**(8), 2856–2861 (1967). https://doi.org/10.1063/1.1712308
6. Bernet, T., Piñeiro, M.M., Plantier, F., et al.: A 3D non-local density functional theory for any pore geometry. Mol. Phys. **118**(9–10), e1767308 (2020). https://doi.org/10.1080/00268976.2020.1767308
7. Bitzek, E., Koskinen, P., Gähler, F., et al.: Structural relaxation made simple. Phys. Rev. Lett. **97**(17), 1–4 (2006). https://doi.org/10.1103/PhysRevLett.97.170201
8. Coasne, B., Pikunic, J., Pellenq, R.M., et al.: Comparison between adsorption in pores of a simple geometry and realistic models of porous materials. MRS Online Proc. Libr. (OPL) **790**, P8-5 (2003). https://doi.org/10.1557/PROC-790-P8.5
9. Corrente, N.J., Hinks, E.L., Kasera, A., et al.: Modeling adsorption of simple fluids and hydrocarbons on nanoporous carbons.

Carbon **197**, 526–533 (2022). https://doi.org/10.1016/j.carbon.2022.06.071
10. Cotterman, R.L., Schwarz, B.J., Prausnitz, J.M.: Molecular thermodynamics for fluids at low and high densities. I: part Pure fluids containing small or large molecules. AIChE J. **32**(11), 1787–1798 (1986). https://doi.org/10.1002/aic.690321104
11. Crawford, B., Timalsina, U., Quach, C.D., et al.: MoSDeF-GOMC: Python software for the creation of scientific workflows for the Monte Carlo simulation engine GOMC. J. Chem. Inf. Model. **63**(4), 1218–1228 (2023). https://doi.org/10.1021/acs.jcim.2c01498
12. de Tomas, C., Suarez-Martinez, I., Vallejos-Burgos, F., et al.: Structural prediction of graphitization and porosity in carbide-derived carbons. Carbon **119**, 1–9 (2017). https://doi.org/10.1016/j.carbon.2017.04.004
13. de Tomas, C., Suarez-Martinez, I., Marks, N.A.: Carbide-derived carbons for dense and tunable 3D graphene networks. Appl. Phys. Lett. **112**(25), 251907 (2018). https://doi.org/10.1063/1.5030136
14. Echeverri Restrepo, S., Andric, P.: ABC-FIRE: accelerated bias-corrected fast inertial relaxation engine. Comput. Mater. Sci. **218**(September 2022), 111978 (2023). https://doi.org/10.1016/j.commatsci.2022.111978
15. Eddaoudi, M., Kim, J., Rosi, N., et al.: Systematic design of pore size and functionality in isoreticular MOFs and their application in methane storage. Science **295**(5554), 469–472 (2002). https://doi.org/10.1126/science.1067208
16. El-Sharkawy, I.I., Mansour, M.H., Awad, M.M., et al.: Investigation of natural gas storage through activated carbon. J. Chem. Eng. Data **60**(11), 3215–3223 (2015). https://doi.org/10.1021/acs.jced.5b00430
17. Evans, R.: Density Functional Theory for Inhomogeneous Fluids I: Simple Fluids in Equilibrium. Lectures at 3rd Warsaw School of Statistical Physics, Kazimierz Dolny (2009)
18. Fu, J., Liu, Y., Tian, Y., et al.: Density functional methods for fast screening of metal–organic frameworks for hydrogen storage. J. Phys. Chem. C **119**(10), 5374–5385 (2015). https://doi.org/10.1021/jp505963m
19. Fu, J., Tian, Y., Wu, J.: Classical density functional theory for methane adsorption in metal–organic framework materials. AIChE J. **61**(9), 3012–3021 (2015). https://doi.org/10.1002/aic.14877
20. Gregg, S., Sing, K.: Adsorption, Surface Area and Porosity, 2nd edn., pp. 195–228. Academic Press, New York (1982)
21. Guénolé, J., Nöhring, W.G., Vaid, A., et al.: Assessment and optimization of the fast inertial relaxation engine (FIRE) for energy minimization in atomistic simulations and its implementation in LAMMPS. Comput. Mater. Sci. (2020). https://doi.org/10.1016/j.commatsci.2020.109584
22. Guo, P., Shin, J., Greenaway, A.G., et al.: A zeolite family with expanding structural complexity and embedded isoreticular structures. Nature **524**(7563), 74–78 (2015). https://doi.org/10.1038/nature14575
23. Hansen, J.P., McDonald, I.R.: Theory of Simple Liquids: With Applications to Soft Matter. Academic Press, New York (2013)
24. Henderson, D.: Fundamentals of Inhomogeneous Fluids. CRC Press, Boca Raton (1992)
25. Hirschfelder, J.O., Curtiss, C.F., Bird, R.B.: Molecular Theory of Gases and Liquids. Wiley, New York (1964)
26. Jagiello, J., Olivier, J.P.: 2D-NLDFT adsorption models for carbon slit-shaped pores with surface energetical heterogeneity and geometrical corrugation. Carbon **55**, 70–80 (2013). https://doi.org/10.1016/j.carbon.2012.12.011
27. Jain, S.K., Pellenq, R.J.M., Pikunic, J.P., et al.: Molecular modeling of porous carbons using the hybrid reverse Monte Carlo method. Langmuir **22**(24), 9942–9948 (2006). https://doi.org/10.1021/la053402z
28. Johnson, J.K., Zollweg, J.A., Gubbins, K.E.: The Lennard–Jones equation of state revisited. Mol. Phys. **78**(3), 591–618 (1993). https://doi.org/10.1080/00268979300100411
29. Kalyuzhnyi, Y., Cummings, P.: Phase diagram for the Lennard–Jones fluid modelled by the hard-core Yukawa fluid. Mol. Phys. **87**(6), 1459–1462 (1996). https://doi.org/10.1080/00268979600100981
30. Kessler, C., Eller, J., Gross, J., et al.: Adsorption of light gases in covalent organic frameworks: comparison of classical density functional theory and grand canonical monte carlo simulations. Microporous Mesoporous Mater. **324**, 111263 (2021). https://doi.org/10.1016/j.micromeso.2021.111263
31. Kierlik, E., Rosinberg, M.L.: Density-functional theory for inhomogeneous fluids: adsorption of binary mixtures. Phys. Rev. A **44**(8), 5025–5037 (1991). https://doi.org/10.1103/PhysRevA.44.5025
32. Kostoglou, N., Koczwara, C., Prehal, C., et al.: Nanoporous activated carbon cloth as a versatile material for hydrogen adsorption, selective gas separation and electrochemical energy storage. Nano Energy **40**, 49–64 (2017). https://doi.org/10.1016/j.nanoen.2017.07.056
33. Li, Y., Yu, J.: New stories of zeolite structures: their descriptions, determinations, predictions, and evaluations. Chem. Rev. **114**(14), 7268–7316 (2014). https://doi.org/10.1021/cr500010r
34. Li, J., Corma, A., Yu, J.: Synthesis of new zeolite structures. Chem. Soc. Rev. **44**(20), 7112–7127 (2015). https://doi.org/10.1039/C5CS00023H
35. Li, Q., Xu, W., Liang, X., et al.: Specific alkali metal sites as co2 traps in activated carbon with different pore size for co2 selective adsorption: GCMC and dft simulations. Fuel **325**, 124871 (2022). https://doi.org/10.1016/j.fuel.2022.124871
36. Liu, L., Nicholson, D., Bhatia, S.K.: Adsorption of CH4 and CH4/CO2 mixtures in carbon nanotubes and disordered carbons: a molecular simulation study. Chem. Eng. Sci. **121**, 268–278 (2015). https://doi.org/10.1016/j.ces.2014.07.041
37. Marks, N.: Modelling diamond-like carbon with the environment-dependent interaction potential. J. Phys. **14**(11), 2901 (2002). https://doi.org/10.1088/0953-8984/14/11/308
38. Marks, N.A., Cooper, N., McKenzie, D., et al.: Comparison of density-functional, tight-binding, and empirical methods for the simulation of amorphous carbon. Phys. Rev. B **65**(7), 075411 (2002). https://doi.org/10.1103/PhysRevB.65.075411
39. Martin, M.G., Siepmann, J.I.: Transferable potentials for phase equilibria. 1. United-atom description of n-alkanes. J. Phys. Chem. B **102**(14), 2569–2577 (1998)
40. Mayo, S.L., Olafson, B.D., Goddard, W.A.: DREIDING: a generic force field for molecular simulations. J. Phys. Chem. **94**(26), 8897–8909 (1990). https://doi.org/10.1021/j100389a010
41. McGreevy, R., Pusztai, L.: Reverse Monte Carlo simulation: a new technique for the determination of disordered structures. Mol. Simul. **1**(6), 359–367 (1988). https://doi.org/10.1080/08927028808080958
42. Merlet, C., Rotenberg, B., Madden, P.A., et al.: On the molecular origin of supercapacitance in nanoporous carbon electrodes. Nat. Mater. **11**(4), 306–310 (2012). https://doi.org/10.1038/nmat3260
43. Myers, A.L., Monson, P.A.: Adsorption in porous materials at high pressure: theory and experiment. Langmuir **18**(26), 10261–10273 (2002). https://doi.org/10.1021/la026399h
44. Neimark, A.V., Lin, Y., Ravikovitch, P.I., et al.: Quenched solid density functional theory and pore size analysis of micro-mesoporous carbons. Carbon **47**(7), 1617–1628 (2009). https://doi.org/10.1016/j.carbon.2009.01.050
45. Nejahi, Y., Barhaghi, M.S., Mick, J., et al.: GOMC: GPU optimized Monte Carlo for the simulation of phase equilibria and physical properties of complex fluids. SoftwareX **9**, 20–27 (2019). https://doi.org/10.1016/j.softx.2018.11.005

46. Nguyen, T.X., Cohaut, N., Bae, J.S., et al.: New method for atomistic modeling of the microstructure of activated carbons using hybrid reverse Monte Carlo simulation. Langmuir **24**(15), 7912–7922 (2008). https://doi.org/10.1021/la800351d
47. Palmer, J., Brennan, J., Hurley, M., et al.: Detailed structural models for activated carbons from molecular simulation. Carbon **47**(12), 2904–2913 (2009). https://doi.org/10.1016/j.carbon.2009.06.037
48. Palmer, J., Llobet, A., Yeon, S.H., et al.: Modeling the structural evolution of carbide-derived carbons using quenched molecular dynamics. Carbon **48**(4), 1116–1123 (2010). https://doi.org/10.1016/j.carbon.2009.11.033
49. Paszke, A., Gross, S., Massa, F., et al.: Pytorch: An imperative style, high-performance deep learning library. In: Advances in Neural Information Processing Systems 32. Curran Associates, Inc., p 8024–8035, (2019) http://papers.neurips.cc/paper/9015-pytorch-an-imperative-style-high-performance-deep-learning-library.pdf
50. Peng, X., Vicent-Luna, J.M., Jin, Q.: Separation of CF 4 /N 2, C 2 F 6 /N 2, and SF 6 /N 2 Mixtures in Amorphous Activated Carbons Using Molecular Simulations. ACS Appl. Mater. Interfaces **12**(17), 20044–20055 (2020). https://doi.org/10.1021/acsami.0c01043
51. Powles, R., Marks, N., Lau, D.: Self-assembly of sp2-bonded carbon nanostructures from amorphous precursors. Phys. Rev. B **79**(7), 075430 (2009). https://doi.org/10.1103/PhysRevB.79.075430
52. Ratajczak, P., Suss, M.E., Kaasik, F., et al.: Carbon electrodes for capacitive technologies. Energy Storage Mater. **16**, 126–145 (2018). https://doi.org/10.1016/j.ensm.2018.04.031
53. Ravikovitch, P.I., Neimark, A.V.: Density functional theory of adsorption in spherical cavities and pore size characterization of templated nanoporous silicas with cubic and three-dimensional hexagonal structures. Langmuir **18**(5), 1550–1560 (2002). https://doi.org/10.1021/la0107594
54. Ravikovitch, P.I., Neimark, A.V.: Density functional theory model of adsorption on amorphous and microporous silica materials. Langmuir **22**(26), 11171–11179 (2006). https://doi.org/10.1021/la0616146
55. Ravikovitch, P.I., Vishnyakov, A., Russo, R., et al.: Unified approach to pore size characterization of microporous carbonaceous materials from n2, ar, and co2 adsorption isotherms. Langmuir **16**(5), 2311–2320 (2000). https://doi.org/10.1021/la991011c
56. Ravikovitch, P.I., Vishnyakov, A., Neimark, A.V.: Density functional theories and molecular simulations of adsorption and phase transitions in nanopores. Phys. Rev. E **64**(1), 011602 (2001). https://doi.org/10.1103/PhysRevE.64.011602
57. Rosenfeld, Y.: Free-energy model for the inhomogeneous hard-sphere fluid mixture and density-functional theory of freezing. Phys. Rev. Lett. **63**(9), 980–983 (1989). https://doi.org/10.1103/PhysRevLett.63.980
58. Rosenfeld, Y., Schmidt, M., Löwen, H., et al.: Fundamental-measure free-energy density functional for hard spheres: dimensional crossover and freezing. Phys. Rev. E **55**(4), 4245–4263 (1997). https://doi.org/10.1103/PhysRevE.55.4245
59. Rosi, N.L., Eckert, J., Eddaoudi, M., et al.: Hydrogen storage in microporous metal–organic frameworks. Science **300**(5622), 1127–1129 (2003). https://doi.org/10.1126/science.1083440
60. Roth, R., Evans, R., Lang, A., et al.: Fundamental measure theory for hard-sphere mixtures revisited: the white bear version. J. Phys. **14**(46), 12063–12078 (2002). https://doi.org/10.1088/0953-8984/14/46/313
61. Sang, J., Wei, F., Dong, X.: Gas adsorption and separation in metal-organic frameworks by PC-SAFT based density functional theory. J. Chem. Phys. **155**(12), 124113 (2021). https://doi.org/10.1063/5.0067172
62. Sauer, E., Gross, J.: Classical density functional theory for liquid-fluid interfaces and confined systems: a functional for the perturbed-chain polar statistical associating fluid theory equation of state. Ind. Eng. Chem. Res. **56**(14), 4119–4135 (2017). https://doi.org/10.1021/acs.iecr.6b04551
63. Sauer, E., Gross, J.: Prediction of adsorption isotherms and selectivities: comparison between classical density functional theory based on the perturbed-chain statistical associating fluid theory equation of state and ideal adsorbed solution theory. Langmuir **35**(36), 11690–11701 (2019). https://doi.org/10.1021/acs.langmuir.9b02378
64. Sermoud, V., Barbosa, G., Barreto, A., Jr., et al.: Quenched solid density functional theory coupled with pc-saft for the adsorption modeling on nanopores. Fluid Phase Equilib. **521**, 112700 (2020). https://doi.org/10.1016/j.fluid.2020.112700
65. Sermoud, V.M., Barbosa, G.D., Soares, E.A., et al.: Exploring the multiple solutions of the classical density functional theory using metadynamics based method. Adsorption **27**(7), 1023–1034 (2021). https://doi.org/10.1007/s10450-021-00327-7
66. Sermoud, V., Barbosa, G., Soares, E.A., et al.: PCP-SAFT density functional theory as a much-improved approach to obtain confined fluid isotherm data applied to sub and supercritical conditions. Chem. Eng. Sci. **247**, 116905 (2022). https://doi.org/10.1016/j.ces.2021.116905
67. Sermoud, V., Barbosa, G., Vernin, N., et al.: The impact of the adsorbent energy heterogeneities by multidimensional-multicomponent PC-SAFT-DFT. Fluid Phase Equilib. **562**, 113546 (2022). https://doi.org/10.1016/j.fluid.2022.113546
68. Sevilla, M., Fuertes, A.B.: Sustainable porous carbons with a superior performance for CO2 capture. Energy Environ. Sci. **4**(5), 1765–1771 (2011). https://doi.org/10.1039/C0EE00784F
69. Soares, EdA.: Pyfire. (2020) https://github.com/elvissoares/PyFIRE
70. Soares, EdA.: Pydftlj. (2023) https://github.com/elvissoares/PyDFTlj
71. Soares, Ed.A., Barreto, A.G., Tavares, F.W.: Classical Density Functional Theory Reveals Structural Information of H2 and CH4 Fluids Adsorbed in MOF-5. arXiv pp 1–9. (2023) arXiv:2303.11384
72. Steele, W.A.: The physical interaction of gases with crystalline solids: I. Gas–solid energies and properties of isolated adsorbed atoms. Surf. Sci. **36**(1), 317–352 (1973). https://doi.org/10.1016/0039-6028(73)90264-1
73. Tang, Y., Lu, B.C.: On the mean spherical approximation for the Lennard–Jones fluid. Fluid Phase Equilib. **190**(1–2), 149–158 (2001). https://doi.org/10.1016/S0378-3812(01)00600-8
74. Tang, Y., Tong, Z., Lu, B.C.: Analytical equation of state based on the Ornstein–Zernike equation. Fluid Phase Equilib. **134**(1–2), 21–42 (1997). https://doi.org/10.1016/S0378-3812(97)00049-6
75. Tao, Y., Kanoh, H., Abrams, L., et al.: Mesopore-modified zeolites: preparation, characterization, and applications. Chem. Rev. **106**(3), 896–910 (2006). https://doi.org/10.1021/cr040204o
76. Tao, Y., Zhang, G., Xu, H.: Grand canonical Monte Carlo (GCMC) study on adsorption performance of metal organic frameworks (MOFs) for carbon capture. Sustain. Mater. Technol. **32**, e00383 (2022). https://doi.org/10.1016/j.susmat.2021.e00383
77. Teo, H.W.B., Chakraborty, A., Kayal, S.: Evaluation of CH4 and CO2 adsorption on HKUST-1 and mil-101 (CR) MOFs employing Monte Carlo simulation and comparison with experimental data. Appl. Therm. Eng. **110**, 891–900 (2017). https://doi.org/10.1016/j.applthermaleng.2016.08.126
78. Thyagarajan, R., Sholl, D.S.: A database of porous rigid amorphous materials. Chem. Mater. **32**(18), 8020–8033 (2020). https://doi.org/10.1021/acs.chemmater.0c03057
79. Thyagarajan, R., Sholl, D.S.: Molecular simulations of CH4 and CO2 diffusion in rigid nanoporous amorphous materials. J. Phys.

Chem. C **126**(19), 8530–8538 (2022). https://doi.org/10.1021/acs.jpcc.2c01609
80. Vallejos-Burgos, F., de Tomas, C., Corrente, N.J., et al.: 3D nanostructure prediction of porous carbons via gas adsorption. Carbon **215**, 118431 (2023). https://doi.org/10.1016/j.carbon.2023.118431
81. VanMegen, W., Snook, I.: Physical adsorption of gases at high pressure: III. Adsorption in slit-like pores. Mol. Phys. **54**(3), 741–755 (1985). https://doi.org/10.1080/00268978500100591
82. Walton, J., Quirke, N.: Modelling the phase behaviour of a fluid within a pore. Chem. Phys. Lett. **129**(4), 382–386 (1986). https://doi.org/10.1016/0009-2614(86)80363-3
83. Wu, J.: Density functional theory for liquid structure and thermodynamics. In: Structure and bonding. Springer, Berlin (2008) https://doi.org/10.1007/430_2008_3
84. Wu, J.: Variational Methods in Molecular Modeling. Springer, Cham (2016)
85. Xy, L., Chen, Y., Mo, Y.: A review of charge storage in porous carbon-based supercapacitors. New Carbon Mater. **36**(1), 49–68 (2021). https://doi.org/10.1016/S1872-5805(21)60004-5
86. Yu, Y.X.: A novel weighted density functional theory for adsorption, fluid–solid interfacial tension, and disjoining properties of simple liquid films on planar solid surfaces. J. Chem. Phys. **131**(2), 024704 (2009). https://doi.org/10.1063/1.3174928
87. Yu, Y.X., Wu, J.: Structures of hard-sphere fluids from a modified fundamental-measure theory. J. Chem. Phys. **117**(22), 10156–10164 (2002). https://doi.org/10.1063/1.1520530